ACS APPLIED MATERIALS & INTERFACES

Research Article

www.acsami.org

Morphology-Controlled Synthesis of Au/Cu_2FeSnS_4 Core–Shell Nanostructures for Plasmon-Enhanced Photocatalytic Hydrogen Generation

Enna Ha,[†] Lawrence Yoon Suk Lee,*[,†] Ho-Wing Man,[†] Shik Chi Edman Tsang,[‡] and Kwok-Yin Wong*[,†]

[†]Department of Applied Biology and Chemical Technology and the State Key Laboratory of Chirosciences, The Hong Kong Polytechnic University, Hung Hom, Kowloon, Hong Kong SAR, China

[‡]Wolfson Catalysis Centre, Department of Chemistry, University of Oxford, Oxford, OX1 3QR, United Kingdom

Supporting Information

ABSTRACT: Copper-based chalcogenides of earth-abundant elements have recently arisen as an alternate material for solar energy conversion. Cu_2FeSnS_4 (CITS), a quaternary chalcogenide that has received relatively little attention, has the potential to be developed into a low-cost and environmentlly friendly material for photovoltaics and photocatalysis. Herein, we report, for the first time, the synthesis, characterization, and growth mechanism of novel Au/CITS core–shell nanostructures with controllable morphology. Precise manipulations in the core–shell dimensions are demonstrated to yield two distinct heterostructures with spherical and multipod gold nanoparticle (NP) cores (Au_{sp}/CITS and Au_{mp}/CITS). In photocatalytic hydrogen generation with as-synthesized Au/CITS NPs, the presence of Au cores inside the CITS shell resulted in higher hydrogen generation rates, which can be attributed to the surface plasmon resonance (SPR) effect. The Au_{sp}/CITS and Au_{mp}/CITS core–shell NPs enhanced the photocatalytic hydrogen generation by about 125% and 240%, respectively, compared to bare CITS NPs.

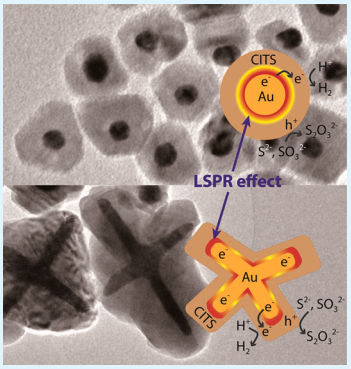

KEYWORDS: *Au/CITS core–shell, surface plasmon resonance, hydrogen evolution, photocatalysis, anisotropic growth*

INTRODUCTION

Nanometer-sized semiconductor sulfides have attracted tremendous attention in the photocatalytic hydrogen production from water, due to their active surfaces and ease of scalable preparation.[1,2] Compared with the photocatalysts based on d^0 metal oxides that are active only under UV, their lower band gap energies offer the advantage of hydrogen generation under visible light. However, poor stability due to photocorrosion and the use of toxic elements have hindered their further developments for wide applications.[3] Recently, research on metal/semiconductor hybrid nanostructures has opened up a new path for enhancing the yield of H_2 production and stabilizing photocatalysts.[4,5] The surface plasmon resonance (SPR) effect[6,7] from plasmonic metal nanoparticles (NPs) influences the neighboring semiconductors via several routes: (1) direct contact injects charge carriers;[8] (2) strong near-field effect generates more excitons;[9] (3) scattering of resonant photons increases optical path length, which accelerates the formation of excited charge carriers.[10] These interactions are most effective in the core–shell configuration where the metal NPs have the maximum interface with semiconductor. Although much effort has been put to make novel metal/semiconductor nanocomposites, fine controlling of the morphology and interface between metal core and semiconductor shell still remains a key challenge to further improve their performances.

Copper-based quaternary chalcogenides have attracted wide attention due to their outstanding photovoltaic and photocatalytic properties.[11] Cu_2FeSnS_4 (CITS) is one of the light-absorbing materials with optimal band gap energy and composed of only earth-abundant, relatively nontoxic, and inexpensive elements. Commonly known as stannite mineral, CITS has a crystal structure closely related to the kesterite structure of Cu_2ZnSnS_4 (CZTS). Their crystal structures are assigned to different space groups only because of different distribution of cations, Cu^+, Zn^{2+}, and Fe^{2+}.[12] Compared with CZTS, which has started to find applications in photocatalysis,[2,13,14] CITS has not been extensively studied, despite having good potential as another eco-friendly photovoltaic material.

For fundamental understanding and better performance in applications, it is crucial to control the morphology of individual metal and semiconductor nanostructures as well as their interface. The delicate tailoring of the size and shape while maintaining a high degree of monodispersity in the preparation of metal/semiconductor hybrid nanomaterials still remains a major challenge. Herein, we report, for the first time, a simple preparation method for novel Au/CITS core–shell nanostructures in which two different preparation conditions were

Received: January 23, 2015
Accepted: April 13, 2015
Published: April 13, 2015

DOI: 10.1021/acsami.5b00715
ACS Appl. Mater. Interfaces 2015, 7, 9072–9077

engaged to control the morphology and yield two distinct shapes: one with a spherical Au NP core (Au_{sp}/CITS) and the other with a multipod Au NP core (Au_{mp}/CITS). The insertion of the Au core into CITS shell has significantly enhanced the photocatalytic hydrogen evolution from both Au_{sp}/CITS and Au_{mp}/CITS core−shell nanostructures.

Au_{sp}/CITS core−shell NPs were synthesized via a seed-mediated method by injecting freshly prepared spherical Au NPs into a solution of Cu−Fe−Sn−oleylamine precursors, whereas Au_{mp}/CITS core−shell NPs were prepared by one-pot synthesis in which Au−oleylamine precursors were nucleated and grown to seeds in the presence of Cu−Fe−Sn−oleylamine precursors at a lower temperature (120 °C). Growth of the CITS shell was initiated by injecting a mixture of 1-dodecanethiol (DDT) and *tert*-dodecanethiol (*t*-DDT) under vigorous stirring at 300 °C. Figure 1 displays typical

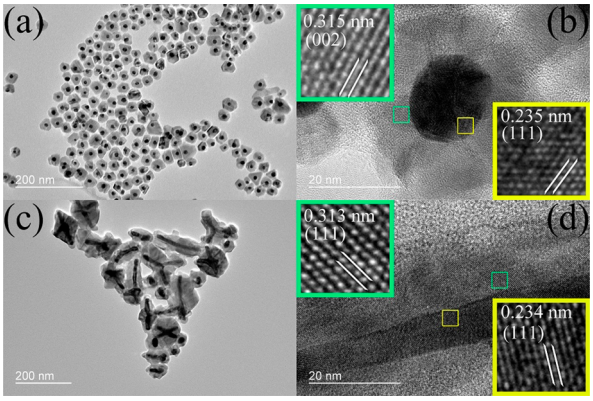

Figure 1. Typical TEM (a, c) and high-resolution TEM (b, d) images of as-synthesized Au_{sp}/CITS (a, b) and Au_{mp}/CITS (c, d) core−shell NPs. (Insets in b and d) Close-up images taken from the core (yellow box) and shell (green box) regions, showing the interlattice *d* spacings.

transmission electron microscopic (TEM) images of Au/CITS core−shell NPs where the clear contrast between Au and CITS reveals two distinct core−shell structures. Highly monodispersed Au_{sp}/CITS core−shell NPs, having an average Au NP core diameter of ca. 10 nm, were covered with CITS shells of which thickness ranged from 10 to 20 nm (Figure 1a). The multipod Au cores, on the other hand, showed an average width of 17 nm and length of 100 nm (Figure 1c). They are not as uniform as those in Au_{sp}/CITS NPs; some of Au NPs are more branched than others. The CITS shell has grown along the Au core, completely covering the Au core to fit the shape of branched Au NP. The thickness of the CITS shell ranged from 10 to 60 nm, with an average of 34 nm based on the measurements of more than 100 NPs.

In order to understand the parameters that control the shape of Au/CITS core−shell NPs in the formation process, it is essential to have detailed data on the crystallographic phase orientations, especially at the heterojunction as it will determine how two dissimilar materials form the interface and grow from there. X-ray powder diffraction (XRD) patterns obtained from as-synthesized Au_{sp}/CITS and Au_{mp}/CITS NPs are shown in Figure S1, Supporting Information. Both NPs exhibit similar diffraction patterns for Au; however, it is interesting to note that the CITS shells possess different crystal phases. In the case of Au_{sp}/CITS NPs, the diffraction peaks appeared at 2θ = 26.9°, 28.5°, 30.3°, 39.1°, 47.6°, 51.3°, 56.3°, and 63.1°, which can be attributed to the (100), (002), (101), (102), (110), (103), (112), and (202) planes of a hexagonal structure, respectively. These peaks match well with those of simulated wurtzite CITS.[15] The three peaks found at 2θ = 38.2°, 44.5°, and 64.6° were assigned to the (111), (200), and (220) lattice planes of cubic Au (JCPDS 04-0784), respectively. A subtle difference was observed from the diffraction pattern of Au_{mp}/CITS NPs, which suggested that the CITS shell is not in the wurtzite structure. Instead, those peaks at 2θ = 28.5°, 33.0°, 47.5°, 56.3°, 59.2°, and 69.2° could be impeccably fitted to the (111), (200), (202), (311), (222), and (400) planes of the simulated cubic zinc blende CITS.[15] Three peaks corresponding to (111), (200), and (220) lattice planes of a cubic Au were found at slightly up-shifted angles of 2θ = 38.5°, 44.7°, and 65.0° (JCPDS 04-0784). The foreign metal ions present during the formation and growth of Au seeds are believed to have interacted with the Au ions and influenced subsequent crystal growth. For example, Fe ions are known to exert a profound effect on directing the anisotropic growth of Au nanomaterials.[16]

A high-resolution TEM image of Au_{sp}/CITS NPs shown in Figure 1b clearly reveals the lattice fringes from both materials, indicating their high degree of crystallinity. The measured interplanar *d* spacings of 0.315 and 0.235 nm can be ascribed to the (002) plane of wurtzite CITS and (111) plane of cubic Au at the materials interface, respectively. The lattice fringes of Au_{mp}/CITS NPs were also clearly observed in the high-resolution TEM image (Figure 1d), where the measured *d* spacings of 0.313 and 0.234 nm are assigned to the (111) plane of zinc blende CITS and (111) plane of cubic Au, respectively. It is noted that the *d* spacing of the Au (111) plane in Au_{mp}/CITS NPs is slightly narrower than that measured from Au_{sp}/CITS NPs. As suggested by XRD results, the incorporation of foreign metal ions during the seed formation step is believed to cause this difference in *d* spacing. No obvious secondary phases or impurity peaks corresponding to binary or ternary sulfides were detected.

The coexistence of four elements in CITS as well as Au was confirmed by energy-dispersive spectroscopy (EDS) and scanning transition election microscopy (STEM) (Figures S2 and S3, Supporting Information). The elemental ratio of Cu:Fe:Sn:S in Au_{sp}/CITS NP was determined to be 2:0.8:1.1:4.4, which corresponds well with its stoichiometric ratio of 2:1:1:4. The Au_{mp}/CITS NPs, however, were found to be iron-deficient; the elemental ratio of Cu:Fe:Sn:S in the CITS shell was determined to be 2:0.6:1:3.9. As reported previously, iron ions are believed to be engaged in directing the anisotropic growth of Au cores in one-pot synthesis, being first reduced to Fe^0 at specific facets of Au.[16] Thus, the amount of Fe precursors available for shell construction in a stoichiometric ratio might be less than the other metal precursors, leading to an overall deficiency in iron in the CITS shell. The elemental mapping identified the even distributions of individual elements in CITS shell as well as the presence of Au in the core.

X-ray photoelectron spectroscopy (XPS) analyses were performed to investigate the oxidation states and composition of surface elements of Au_{sp}/CITS and Au_{mp}/CITS NPs (Figure S4, Supporting Information). From both samples, the XPS survey spectrum identified the presence of all the compositional elements of Au/CITS. The two peaks located at 932 and 951.8 eV corresponded to $2p_{3/2}$ and $2p_{1/2}$ of Cu(I). Two oxidation states of Fe were identified with Fe(II) being the majority state, the peaks of which were located at 720.5 and 708.1 eV, respectively. The other characteristic peaks at 724.1 and 711 eV

DOI: 10.1021/acsami.5b00715
ACS Appl. Mater. Interfaces 2015, 7, 9072−9077

were from Fe(III), which might be formed by exposure to air during the purification step. The narrow Sn 3d peaks that appeared at 486.1 and 494.6 eV with its characteristic peak separation of 8.5 eV confirmed the Sn(IV) state. The sulfur $2p_{3/2}$ and $2p_{1/2}$ peaks were confirmed at 161.6 and 162.8 eV, which agreed with the sulfide phase in the range of 160 and 164 eV. Two single peaks of Au $4f_{7/2}$ and Au $4f_{5/2}$ appear at 84.1 and 87.8 eV, which are consistent with Au^0 in the metallic state.[17,18] The higher intensities of Au^0 peaks from Au_{mp}/CITS NPs indicate that there are more Au^0 on the surface of Au_{mp}/CITS NPs than that of Au_{sp}/CITS NPs. This difference in Au^0 population on the NP surfaces arises from different synthetic procedures. The Au_{sp}/CITS NP was synthesized by growing CITS shell on the preformed Au NPs that acted as nuclei, whereas the Au core in Au_{mp}/CITS NP was prepared by an in situ growing method where the Au precursors unused for seed formation could remain in solution and eventually deposited onto the CITS surface. This doping of Au is not possible under the synthetic conditions for Au_{sp}/CITS NPs, and thus, the detected very weak Au signal of Au_{sp}/CITS NPs is believed to come from a very small fraction of partially exposed Au cores due to incomplete CITS shell.

A comparison of the UV−vis spectra obtained from Au_{sp}/CITS and Au_{mp}/CITS NPs with those of Au NPs and CITS NPs is shown in Figure S5, Supporting Information. The SPR absorption peak of Au in Au_{sp}/CITS NPs exhibits a red shift from its normal position of 525 to 750 nm. The formation of a CITS shell surrounding Au core introduced a high dielectric constant of low band gap CITS to the composite materials.[19] The SPR effect is obvious when the UV−vis spectra of CITS and Au/CITS NPs are compared. The pristine CITS NPs displayed a monotonic increase in absorption intensity from ca. 1100 nm, whereas Au_{sp}/CITS NPs exhibited a much broadened peak between 650 and 1100 nm, suggesting an enhanced absorption range in the vis−NIR region due to extensive perturbation of energy states by the plasmonic field.[20] The broad peak centered at ∼470−500 nm in the Au/CITS spectra can be attributed to CITS shell absorption, which has shifted from the ∼410 nm peak absorption of CITS NPs. The insertion of multipod Au core also induced a wide absorption band between 500 and 1100 nm. Since Au_{mp}/CITS NPs are rather polydispersed with different numbers and lengths of branch of Au core as well as a small population of spherical Au NPs, this broadening in the SPR peak was anticipated as a combination of individual Au cores that exhibit SPR peaks according to their sizes and shapes.[21−23] For instance, the absorption peak at 520 nm gets broader and shifted to 580 nm when the size of Au NP increases from 10 to 100 nm, and a broad peak in the range of 650−850 nm has been reported for Au tetrapods.[23] Moreover, doping of another metal ion was reported to affect the SPR position of Au NPs. The SPR peak in Au−Cu alloy NPs was shown to be tunable from 510 to 900 nm by varying the ratio between Au and Cu.[21]

Intrigued by the unusual shapes of the multipod Au core, we decided to investigate the growth mechanism of Au/CITS using TEM and EDS measured at different reaction temperatures. Figure 2 compares the TEM images of Au_{sp}/CITS NPs taken at various stages of synthesis, and the compositions at each stage are summarized in Figure S6 and Table S1, Supporting Information. At 140 °C, the injected Au NPs were found to have about 14% of Cu with no signs of a new interface or appearance of Cu NP phase, suggesting that Au−Cu alloy was formed (Figure 2a). When the temperature was raised to

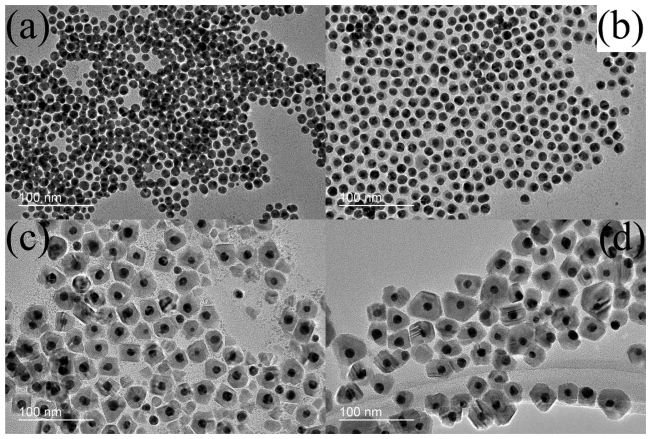

Figure 2. TEM images of Au_{sp}/CITS core−shell NPs obtained at various reaction temperatures of (a) 140, (b) 200, (c) 240, and (d) 300 °C.

200 °C in order to initiate the formation of CITS, Cu_2S was observed to partially cover the Au NP core (Figure 2b). At a further increased temperature of 240 °C, the CITS shell has completely encapsulated the Au core (Figure 2c). The substitution of Cu with Sn and Fe in the shell has converted previously observed Cu_2S to CITS. At this stage, some unreacted binary or ternary sulfides were also observed. The stoichiometric ratio of the CITS shell was obtained only when the reaction temperature was raised to 300 °C, and all intermediate binary or ternary sulfides had been consumed for the growth of the CITS shell (Figure 2d). Apparently, the growth of Au_{sp}/CITS NP starts with the formation of a thin layer of Au−Cu alloy on the Au seed, followed by the adsorption of Cu_2S through the reaction of Cu and DDT. At higher temperature, the substitution of Cu with Sn and Fe produces CITS. A similar growth mechanism was reported for the growth of Au/Cu_2InSe_3 core−shell NPs, CZTS NPs, and $CuInS_2$ NPs.[24−26] In the case of Au_{mp}/CITS core−shell NPs, multipod Au seeds were formed after 10 min of reaction at 120 °C (Figure 3a). These Au seeds, mostly tetrapod and some star shaped, were doped with about 15% Cu, 5% Fe, and 5% Sn (Figure S7 and Table S2, Supporting Information). The crystallographic compression of lattice, due to the existence of these atoms with smaller radii than Au, is believed to

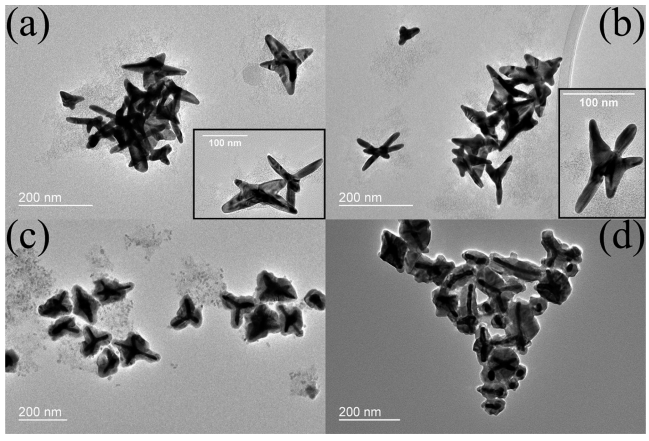

Figure 3. TEM images of Au_{mp}/CITS core−shell NPs obtained at various reaction temperatures (a) after 10 min reaction at 120, (b) 200, (c) 240, and (d) 300 °C.

DOI: 10.1021/acsami.5b00715
ACS Appl. Mater. Interfaces 2015, 7, 9072−9077

contribute to the up-shifting of the XRD signal. At a reaction temperature of 200 °C, the Au multipods grew larger and some noncrystalline particulates populated in their proximity (Figure 3b). In contrast to the case of Au_{sp}/CITS, no Cu_2S was detected from the shell at this stage. Further increasing the temperature to 240 °C enabled the growth of a CITS intermediate shell with more binary or ternary sulfides formed as well (Figure 3c). Finally, all intermediate sulfides had been consumed for the formation of CITS when the temperature was raised to 300 °C (Figure 3d), similar to the case of Au_{sp}/CITS NPs.

The mechanism of multipod Au core formation was further investigated by a series of control experiments in which Au NP core was prepared in the presence of only one or two metal precursors (Figure S8, Supporting Information). The addition of Cu precursors did not give multipod Au NPs but Au NPs with polyhedral shape and clear twinning boundaries (Figure S8a, Supporting Information), which is the result of thermodynamic preference as previously reported.[21] Surprisingly, the addition of Fe precursors alone did not induce the growth of multipods, and only spherical Au NPs were obtained (Figure S8b, Supporting Information). Similar spherical Au NPs resulted in the presence of Sn precursors (Figure S8c, Supporting Information). The formation of multipod Au NP was not triggered by any single metal ion. However, anisotropic growth of Au NPs was observed with the combinations of Cu + Fe and Cu + Sn precursors, as shown in Figure S8e and S8f, Supporting Information, whereas the addition of Fe + Sn precursors only yielded spherical Au NPs (Figure S8d, Supporting Information).

In general, it is more difficult for precious metals with a face-centered cubic unit cell to form a branched multipod nanostructure, compared to semiconductor nanostructures where branched anisotropic growth is possible via polymorphism of the crystal structure. There are a limited number of methods reported on the preparation of multipod Au NPs, including (a) a seed-mediated method where highly faceted Au NP seeds were formed with surfactants such as sodium dodecyl sulfate or cetyltrimethylammonium bromide and transformed into branched nanocrystals by the addition of ascorbic acid,[27,28] (b) template-directed method,[29] and (c) galvanic replacement with Pt(II)[30] or Fe(III)[16] redox couples which provide a localized high concentration of Au adatoms. Most of the multipod Au NPs reported have larger centers with relatively short branches, unlike our case where longer branches were observed. On the basis of our observations, we believe that the formation of multipod Au NPs is first initiated by the interaction with Cu precursors, as Cu ions are known to affect the growth of metal NPs such as Au and Pd via underpotential deposition.[31,32] It is further assisted by Fe and Sn cations to induce the anisotropic growth of Au NPs. In a separate experiment where Zn was used instead of Fe, keeping all other conditions the same, no multipod Au nanostructures were observed. This leads us to believe that the Fe ion, with a synergetic effect from Sn ion, plays a key role in directing overgrowth of Au NPs to multipod shape, which is a thermodynamically unfavorable state with higher surface energy.

Comparative experiments on the photocatalytic H_2 evolution were conducted using zinc blende CITS NPs, Au_{sp}/CITS, and Au_{mp}/CITS core−shell NPs. Figure 4a summarizes the results of 10 mg of CITS (diameter = 14.5 ± 1.3 nm), Au_{sp}/CITS (core diameter = 11.2 ± 1.2 nm, shell thickness = 11.6 ± 2.1 nm), and Au_{mp}/CITS NPs (core length = 99.6 ± 27 nm, core width = 17.2 ± 3.7 nm, shell thickness = 34.3 ± 11.6 nm) under 1 h illumination of visible light with a xenon lamp. About 125% and 240% enhancements in photocatalytic H_2 evolution were observed from Au_{sp}/CITS and Au_{mp}/CITS NPs, respectively, compared to bare CITS NPs. These results are consistent with the enhancement observed in Au/CZTS core−shell NPs.[20] We noted that the CITS shell in Au_{sp}/CITS NPs has wurtzite crystal phase, whereas that in Au_{mp}/CITS has zinc blende phase. In order to investigate the effect from the crystal phase, a control experiment was carried out in which CITS NPs of wurtzite and zinc blende phase were prepared and their photocatalytic activities in H_2 production were compared. Almost no difference was observed between the two crystal phases of CITS NPs, suggesting that the crystal phase does not play a significant role (Figure S11, Supporting Information). Metal doping in semiconductors is known to alter their band structures, which is often used to optimize the optical and photocatalytic properties. The presence of metal atoms or metal NPs on the surface of a semiconductor can also dramatically improve the catalytic activity as they can act as active catalytic sites.[33] Our XPS results indicated the CITS shell of Au_{mp}/CITS NPs is doped with Au of about 0.18% in atomic percentage. Another control experiment was performed to test if the presence of Au on the surface can contribute to the enhancement in photocatalytic activity of CITS NPs. The CITS NPs decorated with Au NPs with an average diameter of 2.5 nm were prepared, and their photocatalytic H_2 evolution was compared with bare CITS NPs under the same conditions (Figure S11, Supporting Information). About 10% enhance-

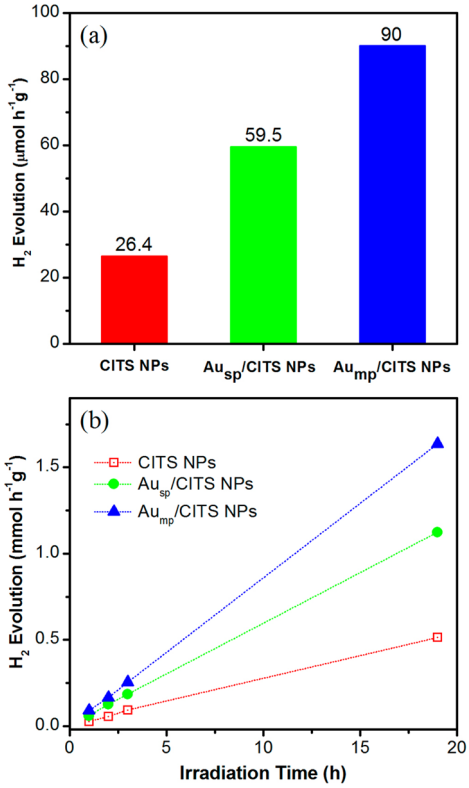

Figure 4. (a) Comparison of the capability of photocatalytic H_2 evolution among zinc blende CITS NPs (red), Au_{sp}/CITS (green), and Au_{mp}/CITS core−shell NPs (blue) after 1 h irradiation. (b) Photocatalytic H_2 evolution over a 19 h reaction by zinc blende CITS NPs, Au_{sp}/CITS, and Au_{mp}/CITS core−shell NPs.

DOI: 10.1021/acsami.5b00715
ACS Appl. Mater. Interfaces 2015, 7, 9072−9077

ment in photocatalytic activity, compared to bare CITS NPs, was observed from Au NP-decorated CITS NPs. This limited enhancement is most probably due to the Au surface which is passivated by dodecanethiol and oleylamine under the experimental conditions employed. Since the doped Au on Au_{mp}/CITS NP surface is expected to have similar surface conditions, being passivated by the same capping ligands, we believe the effect of Au doping is not the major contribution to the observed enhancement in our case.

Ruling out these possible effects, the inserted Au NP core is believed to broaden the light absorption and induced a strong SPR effect. It is worth mentioning that the photocatalytic reaction can be accelerated by either charge transfer from the plasmonic Au core to the CITS shell in the hot electron injection form[5] or exciton concentration induced by a near field effect.[6] Although the exact band structure of CITS is still unknown, it was proposed to have a similar band structure as for CZTS in a recent report where the structural transition and band gap tuning of $Cu_2(Zn,Fe)SnS_4$ were studied.[34] A similar charge transfer mechanism as reported for Au/CZTS NPs[20] may also be engaged in the photocatalytic reactions by Au/CITS NPs, where the excited plasmonic electrons from Au are transferred to the conduction band of CITS.

A rough estimation indicated that the interfacial area between the Au core and the CITS shell per unit weight in Au_{mp}/CITS NPs is only one-half of that in Au_{sp}/CITS, because of the increased Au core dimensions. Interestingly, despite this decrease in contacting surface area and hence narrower charge transfer path, Au_{mp}/CITS NPs showed higher photocatalytic activity than Au_{sp}/CITS NPs. We believe that the increased size and anisotropic shape of a multipod Au core would generate a more intense localized electric field upon irradiation of light with plasmon resonance frequency.[4,5] Thus, the observed enhancements in photocatalytic activity can be better explained with near-field effects of SPR, which result in a faster rate of exciton generation near the CITS surface. Finally, the stability of CITS and Au/CITS core−shell NPs was investigated in a prolonged 19 h reaction (Figure 4b). The hydrogen yield from both CITS and Au/CITS core−shell NPs showed a linear correlation with reaction time. More importantly, all CITS and Au/CITS core−shell NPs maintained their catalytic activities until the end of 19 h reactions, demonstrating their high photocatalytic stabilities.

CONCLUSIONS

We demonstrated that high-purity Au/CITS core−shell NPs with controllable morphology can be achieved by careful tuning of experimental conditions. An Fe/Sn-assisted growth mechanism was discussed for the formation of a multipod Au core. Among the nanomaterials tested, the Au_{mp}/CITS NPs yielded the best vis/NIR-light-driven catalytic activity for hydrogen generation, which can be attributed to the stronger SPR effect.

ASSOCIATED CONTENT

Supporting Information

Details of experiments and additional figures and tables as described in the text. This material is available free of charge via the Internet at http://pubs.acs.org.

AUTHOR INFORMATION

Corresponding Authors

*E-mail: lawrence.ys.lee@polyu.edu.hk.
*E-mail: kwok-yin.wong@polyu.edu.hk.

Notes

The authors declare no competing financial interest.

ACKNOWLEDGMENTS

We acknowledge the support from the Innovation and Technology Commission and the Hong Kong Polytechnic University. K.Y.W. acknowledges the support from the Patrick S. C. Poon Endowed Professorship. E.H. acknowledges the award of a Hong Kong Ph.D. Fellowship administered by the University Grants Committee.

REFERENCES

(1) Lukowski, M. A.; Daniel, A. S.; English, C. R.; Meng, F.; Forticaux, A.; Hamers, R. J.; Jin, S. Highly Active Hydrogen Evolution Catalysis from Metallic WS_2 Nanosheets. *Energy Environ. Sci.* **2014**, *7*, 2608−2613.

(2) Wang, L.; Wang, W.; Sun, S. A Simple Template-Free Synthesis of Ultrathin Cu_2ZnSnS_4 Nanosheets for Highly Stable Photocatalytic H_2 Evolution. *J. Mater. Chem.* **2012**, *22*, 6553−6555.

(3) Chen, X.; Shen, S.; Guo, L.; Mao, S. S. Semiconductor-Based Photocatalytic Hydrogen Generation. *Chem. Rev.* **2010**, *110*, 6503−6570.

(4) Linic, S.; Christopher, P.; Ingram, D. B. Plasmonic-Metal Nanostructures for Efficient Conversion of Solar to Chemical Energy. *Nat. Mater.* **2011**, *10*, 911−921.

(5) Jiang, R.; Li, B.; Fang, C.; Wang, J. Metal/Semiconductor Hybrid Nanostructures for Plasmon-Enhanced Applications. *Adv. Mater.* **2014**, *26*, 5274−5309.

(6) AbouZeid, K. M.; Mohamed, M. B.; El-Shall, M. S. Hybrid Au−CdSe and Ag−CdSe Nanoflowers and Core−Shell Nanocrystals via One-Pot Heterogeneous Nucleation and Growth. *Small* **2011**, *7*, 3299−3307.

(7) Awazu, K.; Fujimaki, M.; Rockstuhl, C.; Tominaga, J.; Murakami, H.; Ohki, Y.; Yoshida, N.; Watanabe, T. A Plasmonic Photocatalyst Consisting of Silver Nanoparticles Embedded in Titanium Dioxide. *J. Am. Chem. Soc.* **2008**, *130*, 1676−1680.

(8) Tian, Y.; Tatsuma, T. Mechanisms and Applications of Plasmon-Induced Charge Separation at TiO_2 Films Loaded with Gold Nanoparticles. *J. Am. Chem. Soc.* **2005**, *127*, 7632−7637.

(9) Seh, Z. W.; Liu, S.; Low, M.; Zhang, S.-Y.; Liu, Z.; Mlayah, A.; Han, M.-Y. Janus Au-TiO_2 Photocatalysts with Strong Localization of Plasmonic Near-Fields for Efficient Visible-Light Hydrogen Generation. *Adv. Mater.* **2012**, *24*, 2310−2314.

(10) Ingram, D. B.; Christopher, P.; Bauer, J. L.; Linic, S. Predictive Model for the Design of Plasmonic Metal/Semiconductor Composite Photocatalysts. *ACS Catal.* **2011**, *1*, 1441−1447.

(11) Aldakov, D.; Lefrancois, A.; Reiss, P. Ternary and Quaternary Metal Chalcogenide Nanocrystals: Synthesis, Properties and Applications. *J. Mater. Chem. C* **2013**, *1*, 3756−3776.

(12) Di Benedetto, F.; Bernardini, G. P.; Borrini, D.; Lottermoser, W.; Tippelt, G.; Amthauer, G. ^{57}Fe− and ^{119}Sn−Mössbauer Study on Stannite (Cu_2FeSnS_4)-Kesterite (Cu_2ZnSnS_4) Solid Solution. *Phys. Chem. Miner.* **2005**, *31*, 683−690.

(13) Wang, P.; Minegishi, T.; Ma, G.; Takanabe, K.; Satou, Y.; Maekawa, S.; Kobori, Y.; Kubota, J.; Domen, K. Photoelectrochemical Conversion of Toluene to Methylcyclohexane as an Organic Hydride by Cu_2ZnSnS_4-Based Photoelectrode Assemblies. *J. Am. Chem. Soc.* **2012**, *134*, 2469−2472.

(14) Arai, T.; Tajima, S.; Sato, S.; Uemura, K.; Morikawa, T.; Kajino, T. Selective CO_2 Conversion to Formate in Water Using a CZTS Photocathode Modified with a Ruthenium Complex Polymer. *Chem. Commun.* **2011**, *47*, 12664−12666.

(15) Zhang, X.; Bao, N.; Ramasamy, K.; Wang, Y.-H. A.; Wang, Y.; Lin, B.; Gupta, A. Crystal Phase-Controlled Synthesis of Cu_2FeSnS_4 Nanocrystals with a Band Gap of Around 1.5 eV. *Chem. Commun.* **2012**, *48*, 4956−4958.

(16) Li, Z.; Tao, J.; Lu, X.; Zhu, Y.; Xia, Y. Facile Synthesis of Ultrathin Au Nanorods by Aging the AuCl(oleylamine) Complex with

DOI: 10.1021/acsami.5b00715
ACS Appl. Mater. Interfaces 2015, 7, 9072−9077

Amorphous Fe Nanoparticles in Chloroform. *Nano Lett.* **2008**, *8*, 3052−3055.
(17) Singh, A.; Geaney, H.; Laffir, F.; Ryan, K. M. Colloidal Synthesis of Wurtzite Cu_2ZnSnS_4 Nanorods and Their Perpendicular Assembly. *J. Am. Chem. Soc.* **2012**, *134*, 2910−2913.
(18) Wang, X.; Xiang, Q.; Liu, B.; Wang, L.; Luo, T.; Chen, D.; Shen, G. TiO_2 Modified FeS Nanostructures with Enhanced Electrochemical Performance for Lithium-Ion Batteries. *Sci. Rep.* **2013**, *3*, 2007.
(19) Falkovsky, L. A. Features of Interband Absorption in the Dielectric Function of Narrow-Gap Semiconductors. *Phys. Rev. B* **2008**, *77*, 193201.
(20) Ha, E.; Lee, L. Y. S.; Wang, J.; Li, F.; Wong, K.-Y.; Tsang, S. C. E. Significant Enhancement in Photocatalytic Reduction of Water to Hydrogen by Au/Cu_2ZnSnS_4 Nanostructure. *Adv. Mater.* **2014**, *26*, 3496−3500.
(21) He, R.; Li, Q.; Zeng, J.; Wang, Y.-C.; Zhou, W.; Wen, L.; Wang, X.; Wang, Z.; Liu, G.; Wang, X.; Hou, J. G.; Chen, X. Facile Synthesis of Pentacle Gold-Copper Alloy Nanocrystals and Their Plasmonic and Catalytic Properties. *Nat. Commun.* **2014**, *5*, 4327.
(22) Lohse, S. E.; Murphy, C. J. The Quest for Shape Control: A History of Gold Nanorod Synthesis. *Chem. Mater.* **2013**, *25*, 1250−1261.
(23) Sau, T. K.; Murphy, C. J. Room Temperature, High-Yield Synthesis of Multiple Shapes of Gold Nanoparticles in Aqueous Solution. *J. Am. Chem. Soc.* **2004**, *126*, 8648−8649.
(24) Regulacio, M. D.; Ye, C.; Lim, S. H.; Bosman, M.; Ye, E.; Chen, S.; Xu, Q.-H.; Han, M.-Y. Colloidal Nanocrystals of Wurtzite-Type Cu_2ZnSnS_4: Facile Noninjection Synthesis and Formation Mechanism. *Chem. Eur. J.* **2012**, *18*, 3127−3131.
(25) Connor, S. T.; Hsu, C.-M.; Weil, B. D.; Aloni, S.; Cui, Y. Phase Transformation of Biphasic Cu_2S−$CuInS_2$ to Monophasic $CuInS_2$ Nanorods. *J. Am. Chem. Soc.* **2009**, *131*, 4962−4966.
(26) Zhang, Q.; Wang, J.-j.; Jiang, Z.; Guo, Y.-G.; Wan, L.-J.; Xie, Z.; Zheng, L. Au-Cu Alloy Bridged Synthesis and Optoelectronic Properties of Au@$CuInSe_2$ Core-Shell Hybrid Nanostructures. *J. Mater. Chem.* **2012**, *22*, 1765−1769.
(27) Kuo, C.-H.; Huang, M. H. Synthesis of Branched Gold Nanocrystals by a Seeding Growth Approach. *Langmuir* **2005**, *21*, 2012−2016.
(28) Chen, S.; Wang, Z. L.; Ballato, J.; Foulger, S. H.; Carroll, D. L. Monopod, Bipod, Tripod, and Tetrapod Gold Nanocrystals. *J. Am. Chem. Soc.* **2003**, *125*, 16186−16187.
(29) Li, Z.; Li, W.; Camargo, P. H. C.; Xia, Y. Facile Synthesis of Branched Au Nanostructures by Templating Against a Self-Destructive Lattice of Magnetic Fe Nanoparticles. *Angew. Chem., Int. Ed.* **2008**, *47*, 9653−9656.
(30) Ortiz, N.; Skrabalak, S. E. Controlling the Growth Kinetics of Nanocrystals via Galvanic Replacement: Synthesis of Au Tetrapods and Star-Shaped Decahedra. *Cryst. Growth Des.* **2011**, *11*, 3545−3550.
(31) Keul, H. A.; Möller, M.; Bockstaller, M. R. Selective Exposition of High and Low Density Crystal Facets of Gold Nanocrystals Using the Seeded-Growth Technique. *CrystEngComm* **2011**, *13*, 850−856.
(32) Chen, Y.-H.; Hung, H.-H.; Huang, M. H. Seed-Mediated Synthesis of Palladium Nanorods and Branched Nanocrystals and Their Use as Recyclable Suzuki Coupling Reaction Catalysts. *J. Am. Chem. Soc.* **2009**, *131*, 9114−9121.
(33) Yu, X.; Shavel, A.; An, X.; Luo, Z.; Ibáñez, M.; Cabot, A. Cu_2ZnSnS_4-Pt and Cu_2ZnSnS_4-Au Heterostructured Nanoparticles for Photocatalytic Water Splitting and Pollutant Degradation. *J. Am. Chem. Soc.* **2014**, *136*, 9236−9239.
(34) Khadka, D. B.; Kim, J. Structural Transition and Band Gap Tuning of $Cu_2(Zn,Fe)SnS_4$ Chalcogenide for Photovoltaic Application. *J. Phys. Chem. C* **2014**, *118*, 14227−14237.

DOI: 10.1021/acsami.5b00715
ACS Appl. Mater. Interfaces 2015, 7, 9072−9077